Xu et al. *NPG Asia Materials* (2024)16:48
https://doi.org/10.1038/s41427-024-00566-4

NPG Asia Materials

ARTICLE Open Access

Burst plasma preparation of metallic nanoparticles on carbon fabrics for antibacterial and electrocatalytic applications

Guiyin Xu[1,2], Zheyi Meng[1], Yunteng Cao[3], Zixu Tao[4], Qing-Jie Li[2], Myles Stapelberg[2], Bing Han[5], Rui Gao[2], Qipeng Yu[2], Meng Gu[5], Benedetto Marelli[3], Hailiang Wang[4], Meifang Zhu[1] and Ju Li[2]

Abstract

Metal nanoparticles have extraordinary properties, but their integration into mesostructures has been challenging. Producing uniformly dispersed nanoparticles attached to substrates in industrial quantities is difficult. Herein, a "plasmashock" method was developed to synthesize metal nanoparticles anchored on different types of carbonaceous substrates using liquid salt solution precursors. These self-supporting, nanoparticle-loaded carbon fabrics are mechanically robust and have been tested as antibacterial substrates and electrocatalysts for reducing carbon dioxide and nitrite. A piece of silver–carbon nanotube paper with a silver loading of ~0.13 mg cm^{-2} treated after a few-second plasmashock presents good antibacterial and electrocatalytic properties in wastewater, even after 20 bactericidal immersion cycles, due to the strong bonding of the nanoparticles to the substrate. The results prove the effectiveness of this plasmashock method in creating free-standing functional composite films or membranes.

Introduction

The utilization of metal nanoparticles (NPs) has implications for the development of new catalysts[1–5], flexible electronics[6], environmental filters[7,8], energy storage/transfer materials[9,10], and antimicrobial substrates[11,12]. For catalysis, the large specific surface area of metal NPs minimizes the use of noble metals[13,14]. This has reduced the cost of catalysts utilizing expensive materials such as Pt, Pd, Rh, Au, and Ag[15]. Furthermore, metal NPs have been applied in filters to remove toxins from aqueous environments due to their large surface areas and unique catalytic activity[16]. In addition, bacteria have been effectively sterilized *via* contact killing, mitigating the effects of bacteria such as *E. coli*[17]. Finally, some aqueous and hybrid-energy storage devices[18] have metallic NPs inside.

Although the aforementioned applications are impressive, the benefits of metallic NPs are partially mitigated if binders are required to fasten them or if the NPs coarsen or aggregate during service[19,20]. To address these practical limitations, research has been conducted to fabricate binder-free metal nanoparticle-decorated films or membranes[21,22]. Ultrahigh-temperature synthesis methods have been widely used to fabricate metallic NPs on substrates. The carbothermal shock method, which allows the rapid conversion from electric to heat energy, has been used to prepare Pt, Ni, and Pd NPs on carbon supports by Hu et al.[23]. Ultrafine silver NPs on carbon nanofibers for lithium metal anodes have also been fabricated by carbothermal shock[24]. Plasma, which is categorized as hot plasma or cold plasma, has also been applied in the fabrication of binder-free metal nanoparticle-decorated substrates[25]. For example, Vu et al.[26] applied dielectric barrier discharge plasma to a polyamide fabric to investigate the effect of the particle size on metallic Ag nanoparticle deposition. However, current processes to manufacture free-standing materials

Correspondence: Hailiang Wang (hailiang.wang@yale.edu) or Meifang Zhu (zmf@dhu.edu.cn) or Ju Li (liju@mit.edu)
[1]State Key Laboratory for Modification of Chemical Fibers and Polymer Materials, College of Materials Science and Engineering, Donghua University, Shanghai 201620, China
[2]Department of Materials Science and Engineering, and Department of Nuclear Science and Engineering, Massachusetts Institute of Technology, Cambridge, MA 02139, USA
Full list of author information is available at the end of the article
These authors contributed equally: Guiyin Xu, Zheyi Meng

are both time-consuming and energy-intensive, as the entire process tends to take from several hours to several days and is composed of a series of complex steps, with little chance to synthesize large enough quantities for industrial use[27–30].

Here, a method to synthesize metal NPs on carbon nanotube papers (CNTPs) *via* burst microwave plasma discharge is reported. The plasma-induced reduction of metal salts on the surface of the CNTP was observed after 5 s, confirming the effectiveness of using the CNTP as both a sharp electrode tip to ionize the argon plasma and a substrate for the uniform dispersion of the metal NPs. Denoted as the "plasmashock" method, this rapid synthesis of free-standing metal NPs was achieved in a low-cost in-house system. To test the effectiveness of our method, the nano-Ag/CNTP thin film, with a NP diameter of 1.0 cm and a silver loading of ~0.13 mg cm^{-2}, was tested against *E. coli* and CO_2 and NO_2^- reduction, and the results revealed good antibacterial and electrocatalytic properties in wastewater.

Results and discussion

Experimental setup

Argon gas is easier to ionize than N_2 because of its lower breakdown electric field of 160 V mm^{-1} *versus* 340 V mm^{-1}. The ease of ionization with argon can be shown experimentally. In the presence of N_2 gas, carbon nanotube paper encourages only localized burning of the plasma (Fig. S1, Video S1). In contrast, argon readily ionizes (Fig. 1A) when exposed to microwaves and various carbon-rich materials, such as carbon nanotube paper (Fig. S2, Video S2), carbon fabrics (Fig. S3, Video S3), and

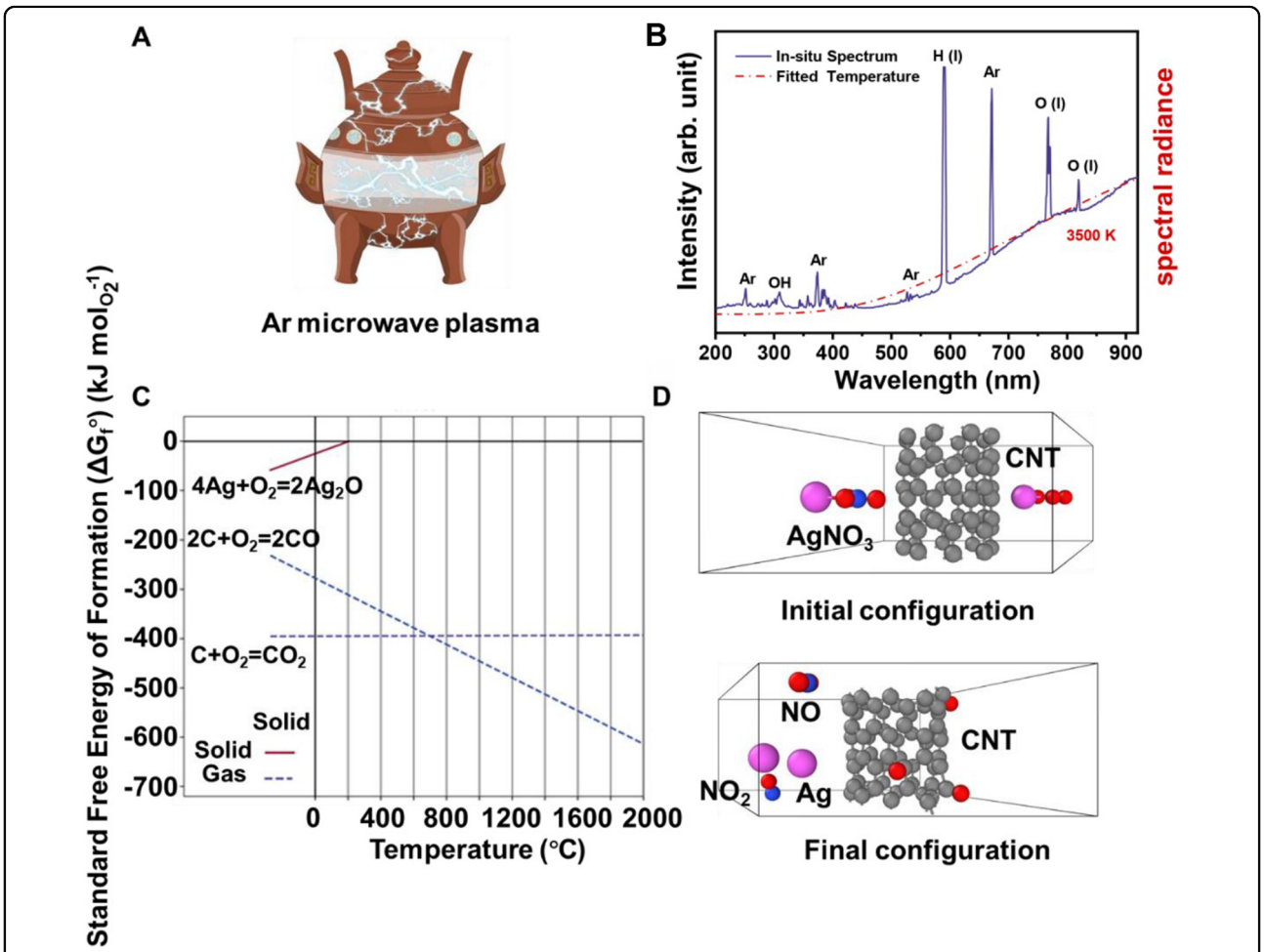

Fig. 1 Synthetic mechanism of Ag atoms on CNTs by Ar microwave plasma. The CNTP induces an Ar microwave plasma at 3500 K, dissociating $AgNO_3$ and obtaining Ag atoms on the CNT. **A** Schematic illustration of carbon-ignited microwave plasma in argon. **B** The in situ spectrum and fitted temperature of carbon nanotube paper exposed to argon and microwave irradiation. **C** Ellingham diagram of silver and carbon[25]. **D** The initial configuration for ab initio molecular dynamics (MD) simulation. The supercell contains two intact $AgNO_3$ molecules and one carbon nanotube (CNT). The dissociation of $AgNO_3$ molecules and oxidization of the CNT occurs at $T = 3500$ K. The CNT is oxidized by the adsorption of O atoms from $AgNO_3$ molecules while reducing $AgNO_3$ molecules to NO, NO_2, and Ag atoms.

carbon nanotube foams (Fig. S4, Video S4). This ionization is further corroborated by the in situ photon spectrum of carbon nanotube paper exposed to argon cover gas and microwave irradiation, which is fitted to Planck's law of black-body radiation (Fig. 1B, Fig. S5)[31]. The fitted temperature reaches ~3500 K in a few seconds. The light-emission spectrum of the Ar plasma based on the double-atom model was further investigated *via* high-level quantum chemistry calculations (Fig. S6, Video S2). The CCSD//6-311++g(3df, 3pd) results indicate that the first excited state emitting ($S_1 \rightarrow S_0$) wavelength is 1411 nm, which is beyond the range of visible light. The second (S_2) and third excited states (S_3) are degenerate states with an emitting wavelength of 654 nm. In addition, the higher excited states S_4 and S_5 generate 526 and 377 nm emitting wavelengths, respectively. Generally, the calculated emission wavelength is in line with the experimental observations (Fig. 1B). The argon plasma has a higher electrical conductivity (0.0025 S m^{-1}) than that of nitrogen plasma (0.00013 S m^{-1}) at 3500 K (Fig. S7)[32]. The argon plasma also has a lower thermal conductivity (0.099 W $(m\,K)^{-1}$) than that of nitrogen plasma (0.20 W $(m\,K)^{-1}$) at 3500 K (Fig. S8). A detailed comparison of the mass density, specific heat capacity, viscosity, enthalpy, and entropy for argon and nitrogen plasma is shown in Figs. S9–13.

The Ellingham diagram of silver and carbon (Fig. 1C) shows that, at a wide range of high temperature, the oxygen–carbon reaction is thermodynamically more favored than the oxygen–silver reaction, suggesting the possibility of obtaining silver NPs by reducing silver nitrate salt particles at local high temperature with carbon materials. To validate our hypothesis, we carried out ab initio MD simulations near 3500 K to investigate the evolution of the $AgNO_3$-CNT system. The initial configuration of our ab initio MD simulation consists of two intact $AgNO_3$ molecules and a CNT (Fig. 1D, Fig. S14A). The temperature was increased from 1 to 3500 K within 10 ps, after which the system was further relaxed for 6 ps. After ~4.5 ps when the heating process had begun, the oxygen atoms started to dissociate from the $AgNO_3$ molecules and were adsorbed by the CNT. These adsorbed oxygen atoms did not detach immediately from the CNT but remained bonded to the CNT over the course of the simulation. As a result, the original $AgNO_3$ molecules were dissociated into NO_x ($x = 1, 2$) and Ag atoms (Fig. 1D, Fig. S14B, Video S5). These reactions are consistent with the trend shown in the Ellingham diagram, thus validating our above hypothesis. Our ab initio MD simulation also indicates that the Ag atoms may further form metal NPs upon cooling.

Characterization of free-standing metal nanoparticle-CNTP

Carbon nanotube paper has high electronic conductivity, excellent mechanical properties, and high thermal conductivity[33]. Carbon nanotube paper was washed with nitric acid to remove residual metal catalysts and impurities (Figs. S15, S16). Then, the treated CNTP was placed in a microwave to ignite the argon plasma (Fig. S17A) for just a few seconds. After the successful testing of Ar-CNTP in the microwave, the CNTP was immersed in aqueous solutions of metal salts (see the "Methods section"). The metal salts adhered to the surface of the CNTP (Fig. S17B). Metal NPs grafted onto the surface of the CNTP within a few seconds after the formation of the argon plasma without additional reducing agents (Fig. S17C).

CNTP is composed of multiwalled carbon nanotubes with a diameter of ~10 nm (Fig. 2A, Fig. S15). The silver NPs are deposited on the surface of the CNTP after the ignition of argon and reduction of $AgNO_3$-CNTP (Fig. 2B, C). A complete reduction of $AgNO_3$ occurs in 5 s, including 3 s to initiate the plasma discharge. The diameter of the silver NPs was observed *via* transmission electron microscopy (TEM) (Fig. 2D, E; Fig. S18), and the particle size was statistically analyzed (Fig. S19): the mean diameter was ~10 nm, with a sigma of 1.22 nm. The elemental mapping images of silver and oxygen are not similar, further indicating that silver NPs are successfully obtained on the CNTP (Fig. 2F–I).

The Young's modulus of CNTP is 794 ± 134 MPa (Table S1), which is in rough agreement with values reported in the literature[34]. The Young's modulus of Ag-CNTP is 1298 ± 141 MPa, which is 63% greater than that of CNTP (Fig. S20). The tensile ductility (by ~77%) and ultimate tensile strength (by ~21%) also decreased. However, the Ag-CNTP composite remains flexible and robust after the fast plasmashock reaction, despite exposure to transient high temperature (Video S6). The X-ray diffraction (XRD) pattern for CNTP (Fig. 3A) shows two main peaks, similar to the (100) and (002) planes for graphite, as our CNTs are multiwalled and have atomic structures similar to those of graphite[35]. After the silver NPs are well grafted on the surface of the CNTP, (111), (200), (220), (311) and (222) diffraction peaks appear in the XRD pattern of Ag-CNTP, corresponding to JCPDS Card No. 87-0597 (face-centered cubic silver)[36]. The presence of the Ag 3d peak in the X-ray photoelectron spectroscopy (XPS) spectra for Ag-CNTP further verifies the presence of silver NPs (Fig. 3B). The C 1 s peak is from the CNTP (Fig. 3C). The O 1 s peak corresponds to the bond between carbon and oxygen (Fig. 3D)[37]. The adsorption of O onto the CNT plays a crucial role in Ag nanoparticle formation[38]. To demonstrate that CNT–O bonding is indeed favored, we carried out both differential charge density analysis and binding energy calculations (Fig. 3E, F). Charge density differences were calculated by subtracting the charge density of the three adsorbed O atoms and the charge density of the remaining atoms (CNT, NO_x and Ag) from that of the entire structure.

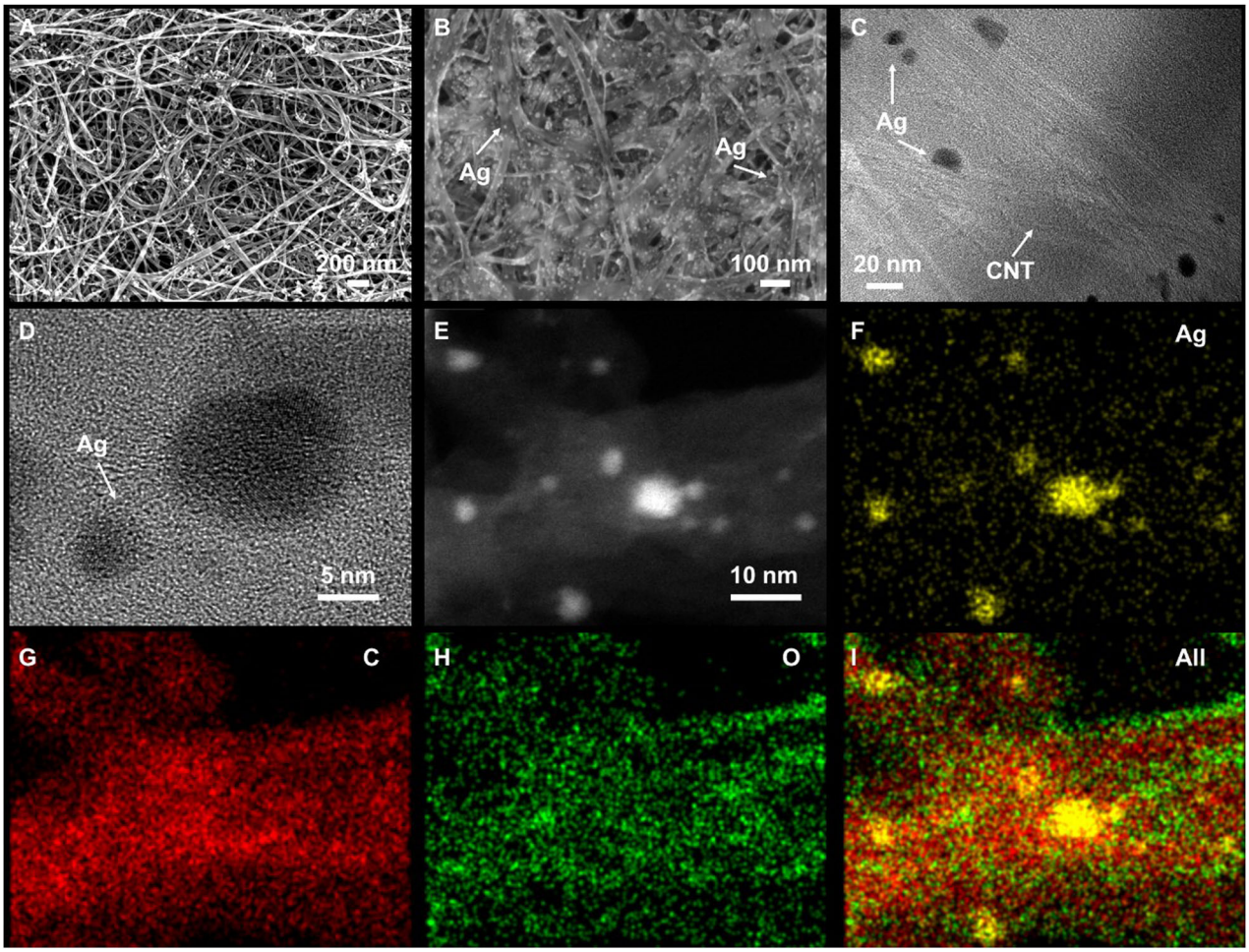

Fig. 2 Ag particles bonded to the CNTP were nanosized and had a uniform distribution. Scanning electron microscopy (SEM) images of (**A**) CNTP and (**B**) Ag-CNTP. **C** Transmission electron microscopy (TEM) and (**D**) high-resolution transmission electron microscopy (HRTEM) images of Ag-CNTP. **E** Scanning transmission electron microscopy (STEM) image of Ag-CNTP and the corresponding elemental mapping images for (**F**) silver, (**G**) carbon, (**H**) oxygen, and (**I**) all mappings superimposed on each other.

The blue isosurface represents electron depletion zones, whereas the yellow isosurface denotes electron accumulation zones (Fig. 3F). The adsorption of O onto the CNT involves considerable charge transfer, with more charges accumulating around O atoms, implying the oxidation of the CNT. The strong bonding between O and the CNT was further verified by binding energy calculations (Fig. 3G–I). We extracted different binding sites from ab initio MD trajectories, such as those in Fig. 3E. The binding energies were calculated by subtracting the potential energy of isolated O and the potential energy of the distorted CNT (Figs. S21, S22) from that of the bound structure. The binding energies of the oxygen atoms on the CNT at the three typical sites (Fig. 3G–I) are −3.15, −2.47, and −5.94 eV, respectively. These relatively large binding energies suggest that the CNTP tends to capture O atoms and should remain relatively stable even at high temperatures.

To test the generality of the plasmashock method for dispersing different metal NPs, silver nitrate salt was replaced with metal chlorides to make gold (Fig. S23A, B), palladium (Fig. S24A, B), platinum (Fig. S25A, B), cobalt (Fig. S26A, B), nickel (Fig. S27A, B), and iron NPs (Fig. S28A, B). These NPs have diameters of ~5–10 nm. The corresponding elemental mapping images demonstrate the presence of metal NPs with trace signatures of chlorine.

Electrocatalytic CO_2 and NO_2^- reduction

Noble-metal NPs such as Ag or Pd NPs on high electrical conductivity carbon substrates may exhibit good performance in electrochemical CO_2 reduction to CO and NO_2^- reduction to NH_4^+[39–41]. $CO + H_2$, also known as syngas, can be directly used to synthesize chemical products *via* the Fischer–Tropsch process[42,43]. NH_4^+ can be

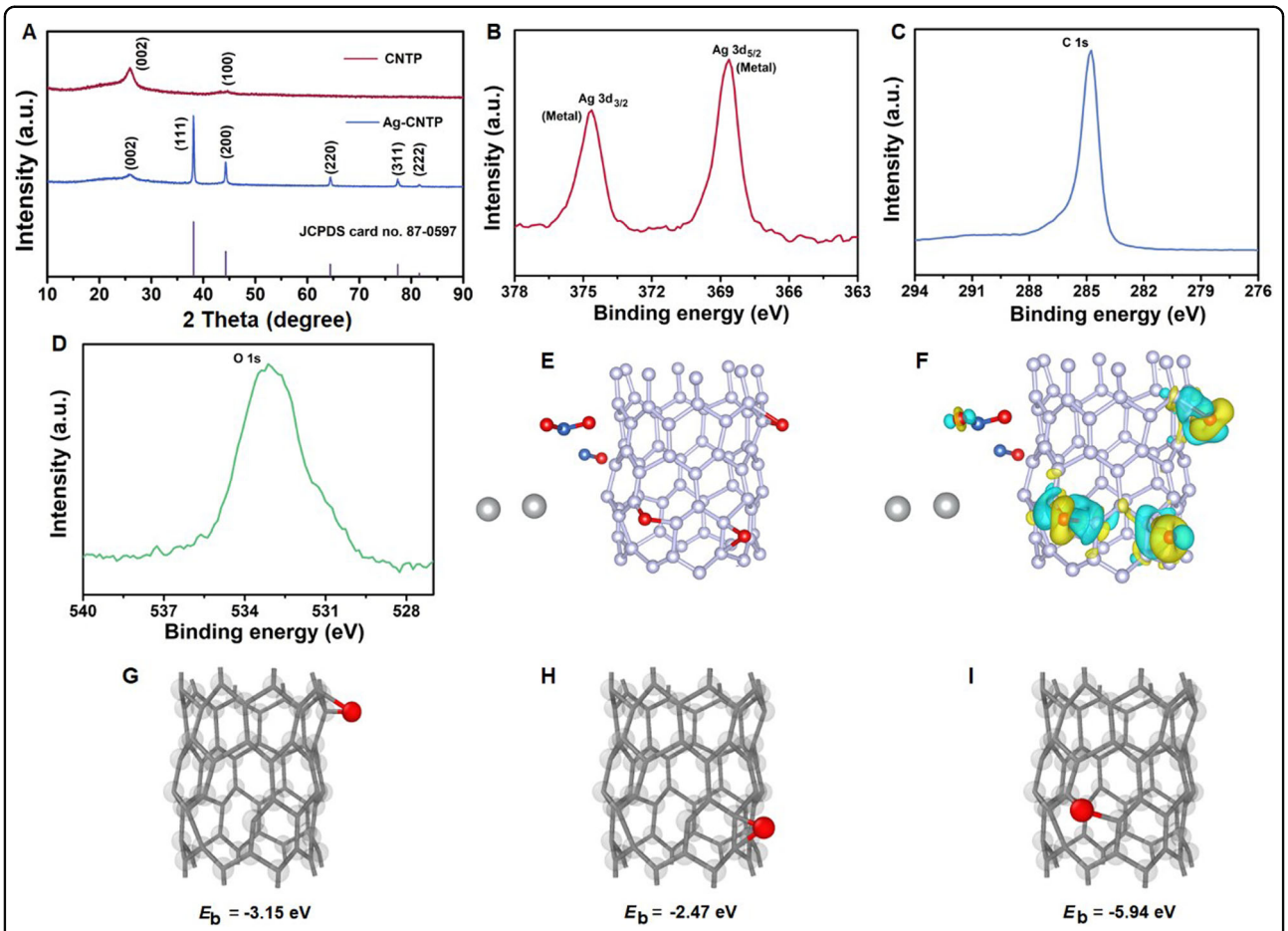

Fig. 3 The binding mechanism of Ag on CNTP. The CNTs absorb O atoms easily to form bonds, facilitating the bonding of Ag and O atoms. **A** X-ray diffraction (XRD) patterns of CNTP and Ag-CNTP. **B** Ag 3d, (**C**) C 1 s, and (**D**) O 1 s X-ray photoelectron spectroscopy (XPS) spectra for Ag-CNTP. **E** Optimized geometries and (**F**) differential charge densities of Ag-CNTP with NO and NO_2. The red, blue, silver, and brown balls represent oxygen, nitrogen, silver, and carbon atoms, respectively. **G**, **H**, **I** Optimized geometries of oxygen on different sites of a CNTP.

used as the main fertilizer in agriculture. Ag-CNTP is capable of catalyzing the two electrochemical reductions mentioned above (Fig. 4A). CO_2 reduction electrolysis was performed in a CO_2-saturated 0.1 M $KHCO_3$ aqueous electrolyte (Figs. 4B, S29, S30). With a total current of 12.5 mA at -1.0 V vs. the reversible hydrogen electrode (RHE), Ag-CNTP showed ~60% and 35% Faradaic efficiency (FE) for H_2 and CO production, respectively. The FE (CO) remained stable during the 10-h stability test (Fig. S31). When NO_2^- reduction electrolysis was performed in an Ar-saturated 0.1 M KNO_2 + 0.1 M $KHCO_3$ aqueous electrolyte, Ag-CNTP exhibited >93% FE (NH_4^+) in the electrode potential range of −0.4 to −0.8 V vs. RHE (Figs. 4C, S32). Compared with previous research on Ag-NP-loaded materials (Table 1), although the FE of Ag-CNTPs for the reduction of CO_2 and NO_2^- is not the highest, considering the facile fabrication, short duration time for silver loading, flexible substrate, and catalysis for transfer from wastewater containing CO_2 and NO_2^- to reusable materials (CO, H_2, and NH_4^+), Ag-CNTP is still a promising catalytic material.

Antibacterial performance

To verify the effectiveness of Ag-CNTPs as antimicrobial materials, the antibacterial activity of the fabricated Ag-CNTP against the gram-negative bacteria *E. coli* ATCC 25922 was investigated (Fig. 5A). A circular disk of Ag-CNTP with a diameter of 1.0 cm and a silver loading of ~0.13 mg cm^{-2} (~19.0 wt% of the total sample) in a 3 mL suspension with a concentration of ~10^4 cells mL^{-1} was used for these tests. Compared with other AgNP-loaded materials (Table 1), Ag-CNTP showed good antibacterial efficacy toward an *E. coli* aqueous suspension, whereby the bacteria lost the ability to reproduce within 10 min. In the control experiment, CNTP itself had no noticeable influence on the viability of the bacteria (Figs. S33, S34). The antibacterial efficacy of Ag-CNTP in repeated use (i.e., after the wash cycle)

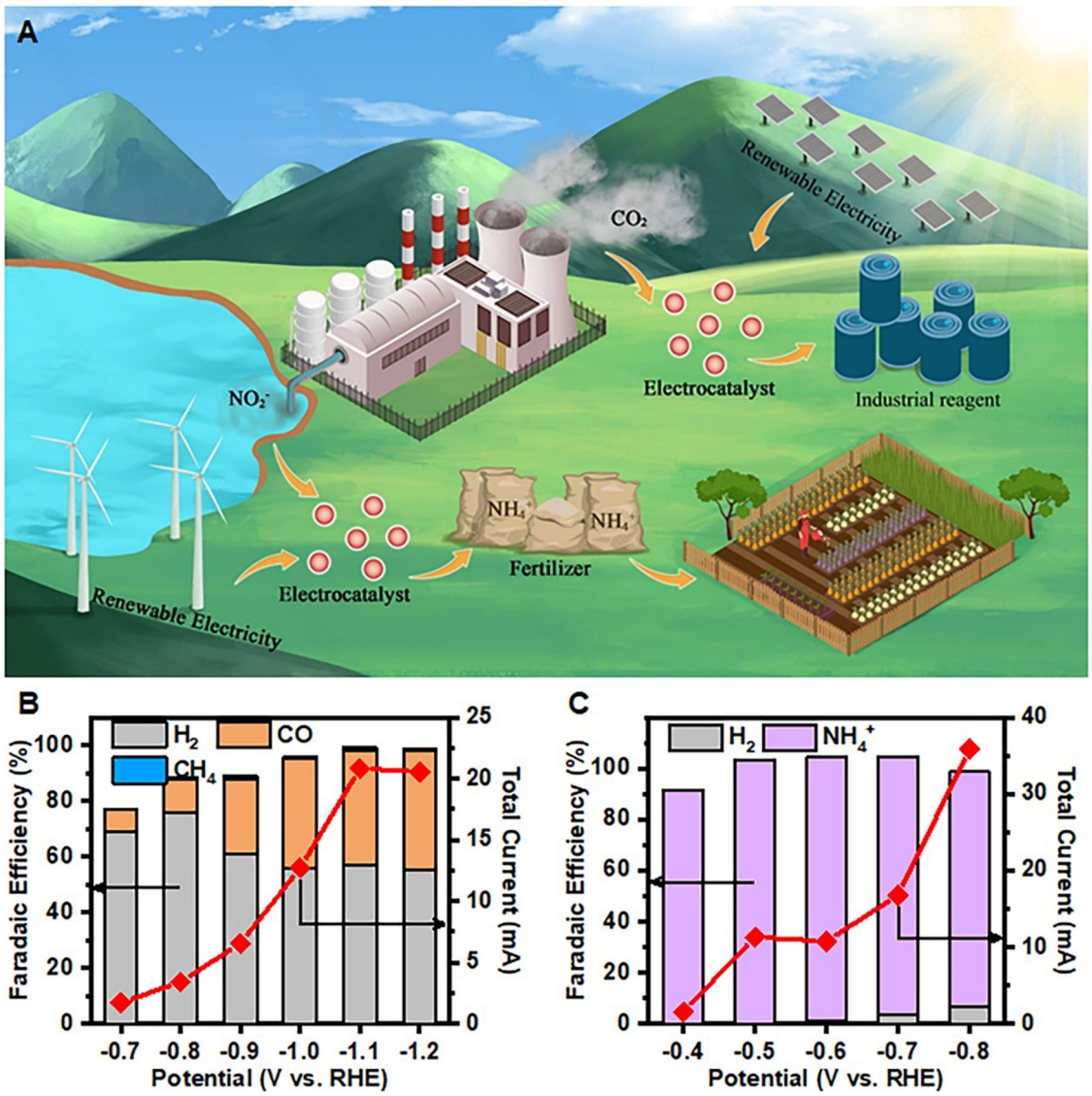

Fig. 4 Ag-CNTP was applied in a green and sustainable way to reduce CO_2 and synthesize ammonia. A Schematic illustration of the Ag-CNTP electrocatalyst for the CO_2/NO_2^- reduction reaction and practical applications. **B** CO_2 reduction electrocatalysis of Ag-CNTP in CO_2-saturated 0.1 M aqueous $KHCO_3$. **C** NO_2^- reduction electrocatalysis of the Ag-CNTP in an Ar-saturated 0.1 M KNO_2 and 0.1 M $KHCO_3$ aqueous electrolyte.

was also investigated. Compared with decorated antimicrobial substrates, immobilized Ag NPs perform better, as the leaching of silver and reusability are minimized and maximized, respectively (Figs. S34, S35)[44,45]. With repeated use, Ag-CNTP displayed decreased antibacterial efficacy, increasing from 10 min to sterilization in its first use to more than 20 min after the tenth time to sterilize the same amount of *E. coli*. However, the Ag-CNTP killed most of the bacteria present (more than 90%) within 40 min and all of the bacteria within 60 min, even after twenty cycles of bactericidal use and washing, demonstrating the high reusability of the Ag-CNTP fabric. As expected, this decrease in antibacterial efficacy may have resulted from the detachment of silver NPs from the CNTP after the bacteria were agitated in suspension, but the loss of silver was expected to be limited (Fig. S35).

According to previous studies, the primary mechanism for the antibacterial properties of the Ag-CNTP, is contact killing[46,47]. Other potential antibacterial mechanisms for free-standing Ag NPs, such as the deactivation of enzymes and ribosomes and denaturation of proteins, may also contribute to the high antimicrobial efficacy of Ag-CNTP but are not dominant (Fig. 5A)[48,49]. To visually observe the antibacterial effect of the Ag-CNTP, the treated bacteria were stained with live/dead fluorescent dyes. The

Table 1 Comparison of the performance, metal loading amount, and loading time of Ag-CNTPs and other Ag NP-loaded materials.

Materials	Application performance	Loading amount of metal nanoparticles	Duration time of metal loading	Ref.
Ag NPs decorated carbon foams	Reduction of CO_2 to CO: FE 84%	57.4 wt%	>16 h	[59]
Thiol-capped Ag NPs deposited on carbon black	Reduction of CO_2 to CO: FE 86.7%	-	>3 h	[60]
Pt/Rh-enzyme complex immobilized on carbon particles	Reduction of NO_2^- to NH_4^+: FE 69%	-	>8 h	[61]
AgNPs/PDA decorated non-woven cotton fabrics	Antibacterial activity against *S. aureus* and *E. coli*	-	>6.5 h	[62]
AgNPs deposited on carbon nanotube carpets functionalized with plasma treatment	Antibacterial activity against *E. coli*	6.6 wt%	>12 h	[63]
AgNPs/rGO decorated cotton fabrics	Antibacterial activity against *E. coli*	13.2 wt%	>20 h	[64]
Ag-CNTPs via plasmashock	Reduction of CO_2 to CO: FE 35% Reduction of NO_2^- to NH_4^+: FE 93% Antibacterial action against *E. coli*	19.0 wt%	5 s	This work

As no instances of Ag NPs electrocatalyzing NO_2^- reduction have been reported, a Pt/Rh NP-loaded material was chosen instead.

bacteria with intact cell membranes were stained green by SYTO 9, whereas bacteria with damaged cell membranes were stained red by propidium iodide. The bacterial concentration was 10^8 cells mL^{-1} to facilitate microscopy. Fluorescent green bacteria were initially observed, with only a few fluorescent red bacteria due to cell death and/or cell membrane damage during bacterial culture or sample preparation (Fig. 5B). After treatment for 4 h, the majority of bacteria were stained red, with only a few stained green, as shown in Fig. 5C, indicating damage to the cell membranes (Fig. 5A). All bacteria were stained red after 8 h of treatment with the Ag-CNTP (Fig. 5D). The viability of bacteria was further tested by colony counting because of the possibility of false-positive viability readings. Fig. 5E–G confirms the results shown in Fig. 5B–D.

Conclusion

Functional metallic nanoparticle–carbon mesostructures were successfully prepared *via* microwave-assisted burst plasma discharging with liquid metal salt solutions dropped on porous carbonaceous substrates. These metal NPs were homogeneously distributed on the surface of the carbon in a short time. Furthermore, as a fabric, Ag-CNTP has good antibacterial and electrocatalytic properties, and these properties survive repeated washing.

Methods

Carbon nanotube paper treatment

The CNTPs were cut into rounds with a diameter of 10 mm. These CNTPs were subsequently soaked in 3 mol L^{-1} nitric acid aqueous solution for 10 h at 60 °C. Finally, the CNTPs were repeatedly washed with deionized water and ethanol and dried at room temperature.

Preparation of metal–carbon nanotube papers

The treated carbon nanotube paper was soaked in 5 mL of 0.05 mol L^{-1} silver nitrate aqueous solution for 1 h and then dried at room temperature for 3 h. The obtained silver nitrate–carbon nanotube paper (Ag-CNTP) circle was placed in a sealed container with argon. The sealed container was put into a household microwave oven with a power output of 1100 W for 5 s. Finally, silver–CNTPs were obtained after washing with deionized water and drying at room temperature. Ni-CNTP, Pt-CNTP, Co-CNTP, Fe-CNTP, Pd-CNTP, and Au-CNTP were obtained by replacing the silver nitrate aqueous solution with nickel chloride, platinum chloride, cobalt chloride, iron chloride, palladium chloride, and gold chloride aqueous solutions.

Materials characterization

In situ light spectrum data were recorded on an FX2000-EX-type fiber optic spectrometer. Scanning electron microscopy (SEM) was performed on a Zeiss Merlin high-resolution scanning electron microscope. TEM and scanning transmission electron microscopy were carried out on a JOEL 2010F instrument. X-ray diffraction (XRD) patterns were recorded on a Rigaku Smartlab multipurpose diffractometer. X-ray photoelectron spectroscopy (XPS) analysis was performed on a Perkin-Elmer PHI 550 spectrometer with Al Kα radiation (1486.6 eV) as the X-ray source.

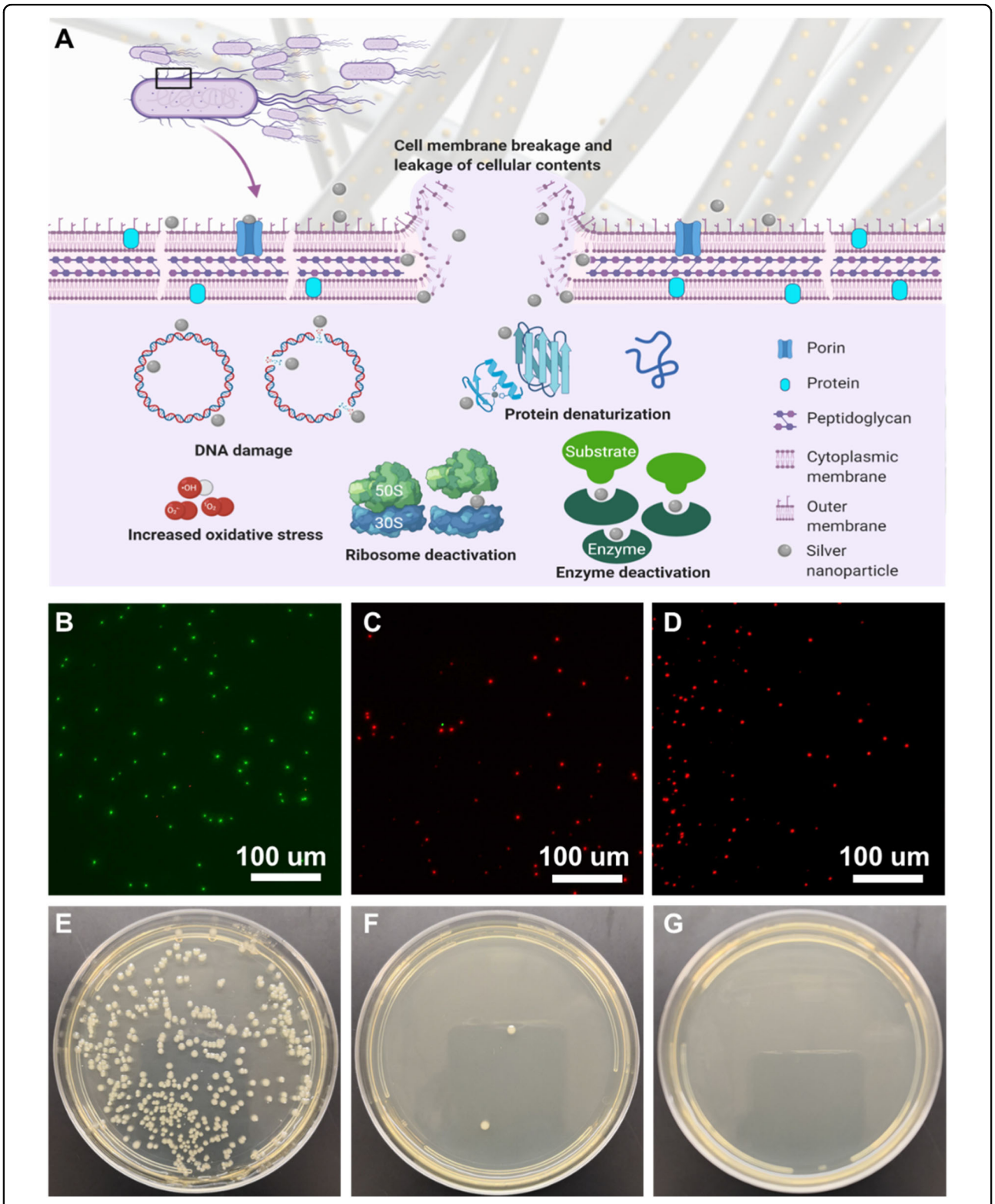

Fig. 5 Ag-CNTP demonstrates effective and stable antibacterial performance. A Schematic diagram of the antibacterial mechanism of Ag-CNTP. Once *E. coli* is exposed to Ag nanoparticles immobilized on the CNTP, the Ag nanoparticles function. Contact killing is considered the predominant antibacterial mechanism for immobilized Ag nanoparticles. Bacterial viability and integrity of the cell membrane after treatment with Ag-CNTP at (**B**) 0, (**C**) 4 h, and (**D**) 8 h. Bacteria with intact cell membranes were stained green and considered alive, while bacteria stained red were dead. **E**, **F**, **G** Are the abilities of the corresponding bacteria to reproduce in suitable nutrient agar. The data are presented as the mean ± s.d. ($n = 3$).

Mechanical performance

The samples were cut into ribbons with dimensions of ~3 mm × 20 mm. The sample width and thickness were extracted from optical images and SEM images, respectively, *via* ImageJ 1.52i. Film tensile experiments were carried out on a dynamic mechanical analysis Q850 model (TA instruments, New Castle, DE) at a rate of 1 mm min^{-1} at room temperature. At least 3 samples were tested for each case.

CO_2 and KNO_2 reduction measurements

With continuous 20 sccm CO_2 bubbling, step-potential electrolysis was performed from −0.7 to −1.2 V at 0.1 V 10 min^{-1} per step. The gas products were subjected to CO_2 flow and analyzed *via* gas chromatography (GC). The gas chromatograph (MG#5, SRI Instruments) was operated with Ar as the carrier gas. The quantification was calibrated by running standard gaseous samples containing known amounts of H_2, CO, and CH_4. With continuous 20 sccm CO_2 bubbling, potentiostatic electrolysis was performed for 10 h at −1.0 V to test the stability of the Ag-CNTP. Formate was the only liquid product, which was quantified after electrolysis by sampling the cathodic compartment electrolyte. A total of 450 µL of post-electrolysis electrolyte was mixed with 50 µL of an internal standard solution containing 50 mM potassium benzoate in D_2O. By comparing the formate proton peak area vs. that of benzoate, the concentration of formatted was determined. Potentiostatic electrolysis was performed in 0.1 M KNO_2 + 0.1 M $KHCO_3$ aqueous solution at each potential for 30 min under a 20 sccm Ar flow. The gas product H_2 was produced by the Ar flow and analyzed by the GC. The liquid product NH_4^+ was quantified after electrolysis *via* a colorimetric method.

Antibacterial test

E. coli ATCC 25922 was cultured overnight as instructed and diluted to an OD600 of 1 with culture media for further use. To investigate the antibacterial activity of Ag-CNTP, the culture (OD600 ~ 1) was centrifuged at 5000 × *g* for 3 min, resuspended in sterile Milli-Q water, and diluted 10^5 to 10^4 cells/mL. Three milliliters of the cell culture mixture was added to a 15-mL Falcon™ round-bottom polystyrene test tube, followed by the addition of one piece of Ag-CNTP with a diameter of 10 mm. The tube was then incubated at 25 °C with shaking at 250 rpm. One hundred microliters of suspension was sampled at prescribed time points, i.e., 10, 20, 40, and 60 min, and then spread on an agar plate. The plate was incubated at 37 °C overnight for colony counting. The experiment was carried out in triplicate. A LIVE/DEAD® BacLight™ Bacterial Viability Kit (Cat. L7012) was used to stain *E. coli*. The bacterial culture was suspended in sterile water after washing and diluted to 2×10^8 cells/mL. A piece of Ag-CNTP was added to the bacterial culture and incubated at 25 °C with shaking at 250 rpm. A 10 µL suspension was sampled after 4 h and 8 h for staining and colony counting.

Simulation

The emission spectrum of the Ar plasma was calculated *via* the CCSD method with a 6-311+g (3d, p) basis set executed in the Gaussian program suite[50]. The double-atom model system was employed to mimic the Ar plasma[51].

Ab initio MD simulations were computed *via* the Vienna Ab initio simulation package (VASP)[52–55]. The generalized gradient approximation, with the Perdew–Burke–Ernzerhof exchange-correlation function[56], was adopted for the exchange–correlation functional. Projector-augmented wave pseudo-potentials[57,58] (versions of C, O, N, and Ag as supplied in the VASP package) were used to model core electrons. The planewave energy cutoff was set as 520 eV. A k-point grid of size 1 × 1 × 3 was used for the Brillouin zone integration. Gaussian smearing with a width of 0.05 eV was used for the partial occupancies of states. All calculations were spin-polarized. Ab initio MD simulations were carried out under the Nose–Hoover thermostat ensemble with a time step of 1 fs. Differential charge difference was carried out by assuming two subsystems, i.e., adsorbed oxygen atoms and the remaining CNT-NO_x-Ag. The binding energies of oxygen with the CNT were calculated according to $E_b = E_{CNT+O} - E_{CNT} - E_O$, with all configurations directly extracted from our ab initio MD simulations.

Acknowledgements

We acknowledge support from the National Natural Science Foundation of China (52103076). G.X. and J.L. would like to acknowledge the support of the Honda Research Institute, USA.

Author details

[1]State Key Laboratory for Modification of Chemical Fibers and Polymer Materials, College of Materials Science and Engineering, Donghua University, Shanghai 201620, China. [2]Department of Materials Science and Engineering, and Department of Nuclear Science and Engineering, Massachusetts Institute of Technology, Cambridge, MA 02139, USA. [3]Department of Civil and Environmental Engineering, Massachusetts Institute of Technology, Cambridge, MA 02139, USA. [4]Department of Chemistry and Energy Sciences Institute, Yale University, West Haven, CT 06516, USA. [5]Department of Materials Science and Engineering, Southern University of Science and Technology, Shenzhen 518055, China

Author contributions

J.L., G.X., and M.Z. conceived the idea and experiments. G.X. prepared the metal–carbon nanotube papers. G.X., Y.C., R.G., B.H., Z.T., and Q.Y. carried out the material characterization. Q.J.L. conducted the simulation. G.X. analyzed the data and wrote the manuscript with Z.M., M.S., Y.C., Z.T., M.G., Q.J.L., B.M., H.W., and J.L. All the authors participated in the manuscript review.

Competing interests

The authors declare no competing interests.

Supplementary information The online version contains supplementary material available at https://doi.org/10.1038/s41427-024-00566-4.

Received: 14 June 2022 Revised: 15 June 2024 Accepted: 19 July 2024
Published online: 04 October 2024

References

1. Li, J. et al. Efficient electrocatalytic CO_2 reduction on a three-phase interface. *Nat. Catal.* **1**, 592–600 (2018).
2. Wang, L. et al. A sulfur-tethering synthesis strategy toward high-loading atomically dispersed noble metal catalysts. *Sci. Adv.* **5**, eaax6322 (2019).
3. Zhang, J. et al. Single platinum atoms immobilized on an MXene as an efficient catalyst for the hydrogen evolution reaction. *Nat. Catal.* **1**, 985–992 (2018).
4. Chen, C. et al. Coupling N_2 and CO_2 in H_2O to synthesize urea under ambient conditions. *Nat. Chem.* **12**, 717–724 (2020).
5. Xu, S. et al. Uniform, scalable, high-temperature microwave shock for nanoparticle synthesis through defect engineering. *Matter* **1**, 759–769 (2019).
6. Ko, Y. et al. Flexible supercapacitor electrodes based on real metal-like cellulose papers. *Nat. Commun.* **8**, 536 (2017).
7. Zhao, H., Qian, L., Guan, X., Wu, D. & Zhao, G. Continuous bulk FeCuC aerogel with ultradispersed metal nanoparticles: an efficient 3D heterogeneous electro-Fenton cathode over a wide range of pH 3-9. *Environ. Sci. Technol.* **50**, 5225–5233 (2016).
8. Zhang, J. et al. Ruthenium nanoparticles supported on CeO_2 for catalytic permanganate oxidation of butylparaben. *Environ. Sci. Technol.* **47**, 13011–13019 (2013).
9. Chao, D. et al. Roadmap for advanced aqueous batteries: from design of materials to applications. *Sci. Adv.* **6**, eaba4098 (2020).
10. Tan, G. et al. Freestanding three-dimensional core-shell nanoarrays for lithium-ion battery anodes. *Nat. Commun.* **7**, 11774 (2016).
11. Linklater, D. P. et al. Antibacterial action of nanoparticles by lethal stretching of bacterial cell membranes. *Adv. Mater.* **32**, 2005679 (2020).
12. Kumar, A., Vemula, P. K., Ajayan, P. M. & John, G. Silver-nanoparticle-embedded antimicrobial paints based on vegetable oil. *Nat. Mater.* **7**, 236–241 (2008).
13. Wang, X. et al. Palladium-platinum core-shell icosahedra with substantially enhanced activity and durability towards oxygen reduction. *Nat. Commun.* **6**, 7594 (2015).
14. Xu, G. et al. Fast heat transport inside lithium-sulfur batteries promotes their safety and electrochemical performance. *iScience* **23**, 101576 (2020).
15. Price pressures on metals. *Nat. Catal.* **2**, 735 (2019).
16. Ghaedi, M. et al. Comparison of silver and palladium nanoparticles loaded on activated carbon for efficient removal of Methylene blue: Kinetic and isotherm study of removal process. *Powder Technol.* **228**, 18 (2012).
17. Chen, C. W. et al. Metal nanobullets for multidrug resistant bacteria and biofilms. *Adv. Drug Deliv. Rev.* **78**, 88 (2014).
18. Yan, Y., Wang, T. Y., Li, X. R., Pang, H. & Xue, H. G. Noble metal-based materials in high-performance supercapacitors. *Inorg. Chem. Front.* **4**, 33 (2017).
19. Shrestha, S., Wang, B. & Dutta, P. Nanoparticle processing: understanding and controlling aggregation. *Adv. Colloid Interface Sci.* **279**, 102162 (2020).
20. Gilbert, B., Ono, R. K., Ching, K. A. & Kim, C. S. The effects of nanoparticle aggregation processes on aggregate structure and metal uptake. *J. Colloid Interf. Sci.* **339**, 285–295 (2009).
21. Divya, K. V. & Abraham, K. E. Ag nanoparticle decorated Sb_2O_3 thin film: synthesis, characterizations and application. *Nano Express* **1**, 020005 (2020).
22. Aysin, F., Yilmaz, A. & Yilmaz, M. Metallic nanoparticle-decorated polydopamine thin films and their cell proliferation characteristics. *Coating* **10**, 802 (2020).
23. Huang, Z. et al. Direct observation of the formation and stabilization of metallic nanoparticles on carbon supports. *Nat. Commun.* **11**, 6373 (2020).
24. Yang, C. et al. Ultrafine silver nanoparticles for seeded lithium deposition toward stable lithium metal anode. *Adv. Mater.* **29**, 1702714 (2017).
25. Nimbekar, A. A. & Deshmukh, R. R. Plasma surface modification of flexible substrates to improve grafting for various gas sensing applications: A review. *IEEE Trans. Plasma Sci.* **50**, 1382–1394 (2022).
26. Vu, N. K., Zille, A., Oliveira, F. R., Carneiro, N. & Souto, A. P. Effect of particle size on silver nanoparticle deposition onto dielectric barrier discharge (DBD) plasma functionalized polyamide fabric. *Plasma Process. Polym.* **10**, 285–294 (2013).
27. Ryoo, R. et al. Rare-earth-platinum alloy nanoparticles in mesoporous zeolite for catalysis. *Nature* **585**, 221–224 (2020).
28. Ramesh, G. V., Porel, S. & Radhakrishnan, T. P. Polymer thin films embedded with in situ grown metal nanoparticles. *Chem. Soc. Rev.* **38**, 2646–2656 (2009).
29. Joo, S. H. et al. Ordered nanoporous arrays of carbon supporting high dispersions of platinum nanoparticles. *Nature* **412**, 169–172 (2001).
30. Chen, L. et al. A robust flow-through platform for organic contaminant removal. *Cell Rep. Phys. Sci.* **2**, 100296 (2021).
31. *Black-body radiation*. https://en.wikipedia.org/wiki/Black-body_radiation.
32. *Database of gas discharge plasma*. http://plasma-data.net/indexelectrical.
33. Meng, F. et al. Electro-induced mechanical and thermal responses of carbon nanotube fibers. *Adv. Mater.* **26**, 2480–2485 (2014).
34. Whitten, P. G., Spinks, G. M. & Wallace, G. G. Mechanical properties of carbon nanotube paper in ionic liquid and aqueous electrolytes. *Carbon* **43**, 1891–1896 (2005).
35. Xu, G. et al. Biomass-derived porous carbon materials with sulfur and nitrogen dual-doping for energy storage. *Green. Chem.* **17**, 1668–1674 (2015).
36. Tang, A. et al. Electrical bistability and negative differential resistance in diodes based on silver nanoparticle-poly (N-vinylcarbazole) composites. *J. Appl. Phys.* **108**, 094320 (2010).
37. Xu, G. et al. Ad hoc solid electrolyte on acidized carbon nanotube paper improves cycle life of lithium-sulfur batteries. *Energy Environ. Sci.* **10**, 2544–2551 (2017).
38. Lu, P. H. et al. Peristalsis-like migration of carbon-metabolizing catalytic nanoparticles. *Extrem. Mech. Lett.* **49**, 101463 (2021).
39. Du, Y. D., Meng, X. T., Wang, Z., Zhao, X. & Qiu, J. S. Graphene-based catalysts for CO_2 electroreduction. *Acta Phys. Chim. Sin.* **38**, 2101009 (2022).
40. Zhou, C. et al. Coupling of Pd nanoparticles and denitrifying biofilm promotes H_2-based nitrate removal with greater selectivity towards N_2. *Appl. Catal. B Environ.* **206**, 461 (2017).
41. Barrabes, N. & Sa, J. Catalytic nitrate removal from water, past, present and future perspectives. *Appl. Catal. B Environ.* **104**, 1 (2011).
42. Xu, G. et al. Self-perpetuating carbon foam microwave plasma conversion of hydrocarbon wastes into useful fuels and chemicals. *Environ. Sci. Technol.* **55**, 6239–6247 (2021).
43. Takamoto, S. et al. Towards universal neural network potential for material discovery applicable to arbitrary combination of 45 elements. *Nat. Commun.* **13**, 2991 (2022).
44. Benetti, G., Cavaliere, E., Banfi, F. & Gavioli, L. Antimicrobial nanostructured coatings: a gas phase deposition and magnetron sputtering perspective. *Mater* **13**, 784 (2020).
45. Valerini, D. et al. Ag functionalization of Al-doped ZnO nanostructured coatings on PLA substrate for antibacterial applications. *Coatings* **12**, 1238 (2020).
46. Rigo, S. et al. Nanoscience-based strategies to engineer antimicrobial surfaces, Palivan. *Adv. Sci.* **5**, 1700892 (2018).
47. Gao, L. et al. Biomimetic biodegradable Ag@Au nanoparticle-embedded ureteral stent with a constantly renewable contact-killing antimicrobial surface and antibiofilm and extraction-free properties. *Acta Biomater.* **114**, 117–132 (2020).
48. Baptista, P. V. et al. Nano-strategies to fight multidrug resistant bacteria-"A Battle of the Titans". *Front. Microbiol.* **9**, 1441 (2018).
49. Dakal, T. C., Kumar, A., Majumdar, R. S. & Yadav, V. Mechanistic basis of antimicrobial actions of silver nanoparticles. *Front. Microbiol.* **7**, 1831 (2016).
50. Frisch, M. J. et al. *Gaussian 16, revision a. 03*. (Gaussian, Inc., 2016.
51. Chen, T. & Manz, T. A. Bond orders of the diatomic molecules. *RSC Adv.* **9**, 17072–17092 (2019).
52. Kresse, G. & Hafner, J. Ab initio molecular dynamics for liquid metals. *Phys. Rev. B* **47**, 558–561 (1993).
53. Kresse, G. & Hafner, J. Ab initio molecular-dynamics simulation of the liquid-metal-amorphous-semiconductor transition in germanium. *Phys. Rev. B* **49**, 14251–14269 (1994).

54. Kresse, G. & Furthmüller, J. Efficiency of ab-initio total energy calculations for metals and semiconductors using a plane-wave basis set. *Comput. Mater. Sci.* **6**, 15–50 (1996).
55. Kresse, G. & Furthmüller, J. Efficient iterative schemes for ab initio total-energy calculations using a plane-wave basis set. *Phys. Rev. B* **54**, 11169–11186 (1996).
56. Perdew, J. P., Burke, K. & Ernzerhof, M. Generalized gradient approximation made simple. *Phys. Rev. Lett.* **77**, 3865–3868 (1996).
57. Blöchl, P. E. Projector augmented-wave method. *Phys. Rev. B* **50**, 17953–17979 (1994).
58. Kresse, G. & Joubert, D. From ultrasoft pseudopotentials to the projector augmented-wave method. *Phys. Rev. B* **59**, 1758–1775 (1999).
59. Ma, S. C., Liu, J. F., Sasaki, K., Lyth, S. M. & Kenis, P. J. A. Carbon foam decorated with silver nanoparticles for electrochemical CO_2 conversion. *Energy Technol.* **5**, 861–863 (2017).
60. Chen, Y. et al. In situ construction of thiol-silver interface for selectively electrocatalytic CO_2 reduction. *Nano Res.* **15**, 3283–3289 (2022).
61. Duca, M., Weeks, J. R., Fedor, J. G., Weiner, J. H. & Vincent, K. A. Combining noble metals and enzymes for relay cascade electrocatalysis of nitrate reduction to ammonia at neutral pH. *Chemelectrochem* **2**, 1086–1089 (2015).
62. Gao, Y. N., Wang, Y., Yue, T. N., Weng, Y. X. & Wang, M. Multifunctional cotton non-woven fabrics coated with silver nanoparticles and polymers for antibacterial, superhydrophobic and high performance microwave shielding. *J. Colloid Interf. Sci.* **582**, 112–123 (2021).
63. Karumuri, A. K., Oswal, D. P., Hostetler, H. A. & Mukhopadhyay, S. M. Silver nanoparticles supported on carbon nanotube carpets: Influence of surface functionalization. *Nanotechnology* **27**, 145603 (2016).
64. Ghosh, S. et al. Fabrication of reduced graphene oxide/silver nanoparticles decorated conductive cotton fabric for high performing electromagnetic interference shielding and antibacterial application. *Fiber Polym.* **20**, 1161–1171 (2019).